

1 **Structural Characterization of the Taltal Segment in Northern Chile Between**
2 **22°S and 26°S Using Local Earthquake Tomography**

3

4 Sergio Leon-Rios¹, Valentina Reyes-Wagner¹, Daniela Calle-Gardella¹, Andreas Rietbrock²,
5 Steven Roecker³, Andrei Maksymowicz⁴ and Diana Comte^{1,4}

6 ¹ Advanced Mining Technology Center, Facultad de Ciencias Físicas y Matemáticas,
7 Universidad de Chile. Chile.

8 ² Geophysical Institute, Karlsruhe Institute of Technology, Germany.

9 ³ Earth and Environmental Sciences, Rensselaer Polytechnic Institute, USA.

10 ⁴ Departamento de Geofísica, Facultad de Ciencias Físicas y Matemáticas, Universidad de
11 Chile. Chile.

12

13 **Keypoints**

14 - Seismic catalog reveals forearc activity and slab dip variations. Vp anomalies in
15 oceanic plate are associated with mid-depth seismic events. The seismic catalog
16 revealed active structures in the forearc, dip changes along the slab and fracturing
17 in the Nazca & South American plates

18

19 - Vp/Vs model uncovers oceanic and continental plate anomalies that influence
20 seismicity, including fault systems and hydration changes

21

22 - Shallow low Vp/Vs (<1.75) correlate with ore deposits; deep high Vp/Vs (>1.80)
23 suggest fluids and melting for the Lastarria volcanic complex

24

25

26

27 **Abstract**

28 Recordings of earthquakes by a temporary deployment of 88 short period seismometers
29 in northern Chile were used to derive regional 3D seismic velocity models for the Taltal
30 segment. We used the Regressive ESTimator (REST) package for event detection and
31 automatic onset estimation of P- and S-wave arrival times to create an earthquake catalog
32 with 23,985 hypocenters. We followed standard acceptability criteria to create a high-
33 quality dataset and inverted for 3D V_p , V_s and V_p/V_s models using local earthquake
34 tomography.

35 Plots of hypocenters from the catalog reveal active structures in the upper crust, dip
36 changes along the slab and fracturing within the oceanic crust. The wavespeed models
37 illuminated several features in both the Nazca and South American plate, including the
38 Atacama fault system on the coastline and the Domeyko Fault System in the forearc.
39 These models also provide evidence for fluid circulation caused by the subducting Taltal
40 ridge on the coast and partial melting feeding a volcanic complex close to the Andes.
41 Anomalously low V_p/V_s ratios (<1.77) are associated with copper mining operations in the
42 area, suggesting that this kind of imaging can be used to characterize the distribution of
43 ore deposits in the area.

44

45 **Plain language summary**

46 We recorded earthquakes in northern Chile with a network of 88 seismometers and used
47 the arrival times of P and S waves to generate 3D wavespeed models of the region. These
48 models reveal several structures in the area, including changes in the angle of the
49 subducting Nazca plate and fractures in the oceanic crust. Among features observed in
50 both the Nazca and South American plates are the Atacama and Domeyko fault systems.
51 We also infer fluid circulation caused by the subducting Taltal ridge and partial melting
52 that is feeding a volcanic complex near the Andes. Low values of the V_p/V_s ratio are
53 associated with copper mining operations in the area and could be used to identify new
54 ore deposits.

55 **Keywords:** Northern Chile, 3D Velocity Models, Tectonic Processes, Local Earthquake
56 Tomography, Seismic Catalog, Continental Forearc

57

58 **1. Introduction**

59 The geologically active margin in northern Chile, where the oceanic Nazca plate subducts
60 beneath the continental South American plate at a relative rate of $\sim 6.0\text{-}7.0$ mm/yr
61 (DeMets et al., 1990, 1994; Angermann et al., 1999; Norabuena et al., 1999; Sella et al.,
62 2002) offers an ideal setting for seismic investigations of the subduction process in
63 tectonically erosive margins. The lack of anthropogenic noise and the dryness of the soil
64 allow for high SNR recordings of seismic signals. A variety of heterogeneities, such as
65 seamounts and ridges on the oceanic crust, along with the prominent peninsulas along the
66 coast, contribute to diverse modes by which stress in the region is accumulated and
67 released. In particular, a number of studies have focused on the large thrust events in the
68 area, such as the M8.0 Antofagasta earthquake in 1995 (Monfret et al., 1995; Ruegg et al.,
69 1996; Delouis et al., 1997), the M7.8 Tocopilla earthquake in 2007 (Delouis et al., 2009;
70 Peyrat et al., 2010; Bejar-Pizarro et al., 2010), and a proposed $M_w \sim 9.5$ earthquake
71 (Salazar et al., 2022) 3800 years ago in the Taltal segment between 22°S and 26°S (Figure
72 1). In the same area, long-term geodetic studies have quantified the degree of seismic
73 coupling (Chlieh et al., 2004; Metois et al., 2013; Metois et al., 2016; Klein et al., 2018) and
74 the capacity of the area to host a large megathrust earthquake (Yañez-Cuadra et al.,
75 2022). Several recent investigations have focused on understanding the sources of
76 seismicity in northern Chile. For example, Mavor et al. (2020) described the kinematics
77 and tectonic evolution of the Taltal Fault, Sippl et al. (2023) used a 15-year seismic catalog
78 to summarize the activity in northern Chile, and Gonzalez-Vidal (personal communication,
79 2023) deployed a temporary network to explore the relations between heterogeneity in
80 the subducting plate and the degree of interplate locking. In terms of seismic imaging of
81 this zone, Husen et al. (2000), together with Haberland and Rietbrock (2001), set
82 foundations for tomographic analysis by deriving seismic velocity and attenuation models,

83 respectively. However, despite all these studies, the tectonic processes at a regional scale
84 - from the coastline to the volcanic arc - have been largely ignored.

85 To investigate the roles that features such as a subducting ridge and crustal faults play in
86 the overall tectonics and in the high intermediate-depth seismicity rate of the Taltal
87 segment, we analyzed data from a passive seismic experiment comprising a large network
88 of seismic sensors. The size and the density of this temporary deployment along with the
89 high rate of seismicity in this area (e.g., CSN technical report for the seismicity in Chile
90 2018, 2019, 2020; www.csn.uchile.cl) facilitates applications of high-resolution imaging
91 using local earthquake tomography (LET). This method uses the arrival times of P- and S-
92 phases generated by local earthquakes to derive 3D seismic velocity models for V_p , V_s and
93 V_p/V_s that highlight the structures and anomalies in the subsurface (e.g., Aki and Lee,
94 1976; Eberhart-Phillips et al., 1986; Thurber et al., 1995). In this study, we apply this type
95 of analysis to investigate the distribution of fluids in the Taltal segment and its potential
96 relation to the seismic activity between and within the oceanic and the continental, plates
97 (e.g., Christensen, 1996; Moreno et al., 2012; Contreras-Reyes et al., 2021). The large
98 amount of seismic data recorded by this deployment allows us to image the main
99 geological structures and areas of fluid circulation that control the seismic activity at
100 shallow- (<30 km) and intermediate-depth (~100-200 km) in the segment.

101

102 **2. Tectonic setting**

103 During the past century, only moderate magnitude earthquakes (7.5-8.5) have been
104 documented in the Taltal segment (Figure 1). These include the intraplate M8.0 Calama
105 earthquake in 1950 (Kausel & Campos, 1992), the M7.7 and M7.6 Taltal earthquakes in
106 1966 (Deschamps, 1980) and 1987 (Ruiz and Madariaga, 2018), the interplate M8.1
107 Antofagasta earthquake in 1995 (Monfret et al., 1995; Ruegg et al., 1996; Delouis et al.,
108 1997) and the interplate M7.7 Tocopilla earthquake in 2007 (Delouis et al., 2009; Bejar-
109 Pizarro et al., 2010; Peyrat et al., 2010); all of them located in the northern part of the
110 segment (22°S-25°S). Only one documented megathrust earthquake struck the southern

111 part of this region in 1922 ($M \sim 8.5$, Willis 1929; Abe 1979; Beck, 1998; Comte et al., 2002b;
112 Kanamori et al., 2019), which, due the absence of megathrust events with $M > 8.5$ in the
113 past (Ruiz and Madariaga, 2018) has led to some authors to refer to this portion of the
114 segment (25°S - 27°S) as atypical for the Chilean margin. At the same time, the
115 multidisciplinary study of Salazar et al. (2022) inferred that, based on the effects on
116 ancient inhabitants, a large earthquake and tsunami occurred ~ 3800 yrs ago, suggesting
117 that the area it is capable of hosting large megathrust earthquakes similar to the 2010
118 Maule and 1960 Valdivia event in other regions of Chile (e.g., Kelleher, 1972; Ruiz &
119 Madariaga, 2018). While megathrusts are infrequent, swarms of seismicity are common in
120 this area (Comte et al., 2002a; Holtkamp et al., 2011; Metois et al., 2016) suggesting that
121 heterogeneities along the plate interface complicate this portion of the Taltal segment.

122 Offshore, irregularities in the bathymetry of the seafloor such as the Mejillones Fracture
123 Zone (MFZ, Maksymowicz 2015) and the Taltal ridge (Figure 1a) have been proposed to
124 cause a seismogenic segmentation in the region that stops the rupture propagation of
125 local megathrust earthquakes (Maksymowicz, 2015). Pasten-Araya et al. (2021) discussed
126 the presence of a splay fault close to the coastline in the region and emphasized the
127 importance of these types of structures for seismic hazards. Onshore (Figure 1a), the
128 region has two main N-S fault systems, the Atacama fault system (AFS) and Domeyko fault
129 system (DFS), that were formed in response to an oblique transfer of subduction stress
130 (Mavor et al., 2020 and reference therein). The upper-crust is further complicated by
131 several other small geological structures with diverse lineaments and length, such as the
132 Mejillones fault (MF), the Taltal fault (TTF), the Calama-Olacapato-El Toro lineament (COT)
133 and others (Figure 1a; Arabasz 1968; Arabasz Jr, 1971). These lithospheric scale features
134 should play a critical role in the behavior of crustal seismicity and in the distribution of
135 abundant porphyry copper deposits (Cooke et al., 2005; Richards, 2016).

136 The volcanic arc in this area is shifted towards the east relative to its position to the north
137 and south (Figure 1a), which has been explained by a region of high-density located below
138 the Salar de Atacama (Götze and Krause, 2002; Schurr and Rietbrock, 2004). Eastward, an
139 analysis of electrical resistivity (Diaz et al., 2012; Pritchard et al., 2018; Kühn et al., 2018;

140 Araya-Vargas et al., 2019) and receiver function studies (Ward et al., 2017; Delph et al.,
141 2017) show two large magmatic bodies, the Altiplano-Puna (APMB) and Lazufre (LMB), are
142 located at the edges of the area of interest, with smaller magmatic bodies in between.

143

144 **3. Data and Methods**

145 *Dataset: The Taltal seismic experiment*

146 The data analyzed in this study were recorded by a temporary network deployed as part
147 of a joint effort between the Advanced Mining Technology Center (AMTC) of Universidad
148 de Chile and the Geophysical Institute from the Karlsruhe Institute of Technology (KIT) of
149 Germany and comprised 84 triaxial short period geophones (3D Geophone HL-6B, 4.5 Hz)
150 and Datacube³ digitizers sampling at 200 Hz. The instruments covered an area of ~127,000
151 km² and operated between March and October 2020 (Figure 1b).

152 *Seismic catalog and onset detection*

153 The seismic traces recorded by the Taltal experiment were processed using the Regressive
154 ESTimator (REST) automatic picking package described in Comte et al. (2019). REST uses
155 the autoregressive approach of Pisarenko et al. (1987) and Kushnir et al. (1990), combined
156 with data windowing procedures suggested by Rawles and Thurber (2015), to generate
157 detections and onset estimates of phase arrivals. The functions used for detection and
158 onset estimation are indifferent to waveform morphology, relying instead on statistical
159 estimates of similarity and predictability between a subset of samples and a
160 representation of background noise. Hypocenters are determined using a grid search
161 location scheme (Roecker et al., 2004; 2006) with travel times calculated in a wavespeed
162 model specified at a 3D distribution of nodes in a spherical coordinate system.

163 In this study, we adopted a reference 1D velocity model based on the results of Husen et
164 al. (1999) for shallow and intermediate depths (0-50 km) and IASP91 (Kenneth & Engdahl,
165 1991) for depths > 50 km. Wavespeeds and travel times are specified on a 3D grid of
166 157,500 nodes separated by 10 km over an area of 700 x 750 km² and 285 km depth.

167 Events included in the inversion were required to have a minimum of 10 phases and an
168 arrival time residual of less than 2.0 s, resulting in an initial catalog of 23,985 earthquakes
169 with 774,989 P- and 667,114 S-wave arrival times with an overall root mean square (RMS)
170 residual of 0.48 s. In carrying out the LET, we further refine the catalog by applying a
171 stricter selection criterion requiring (1) an azimuthal gap in recording stations of less than
172 210°, (2) a minimum of 20 total phases, and (3) a maximum residual of 1.5 s. The refined
173 catalog contains 12,851 earthquakes with 415,425 P and 358,770 S arrival times.

174 *Three-dimensional seismic velocity models*

175 The arrival times in the refined catalog were used to generate a 3D velocity model for Vp
176 and Vp/Vs using the joint inversion methodology described in Roecker et al. (2004, 2006).
177 The algorithm parametrizes the subsurface as a volumetric grid in a spherical coordinate
178 system and performs an iterative process that jointly inverts for earthquake locations, Vp,
179 and either Vs or Vp/Vs. The process stops after the reduction in the residual variance
180 becomes statistically insignificant.

181 The grid has 677,376 nodes spaced at 5 km and covers an area of 540 x 560 km² and from
182 the surface to a depth of 270 km. The initial Vp model is the same 1D model used to
183 generate the catalog, and an initial Vp/Vs of 1.77 estimated from a Wadati diagram
184 (Wadati et al., 1933; Kisslinger and Engdahl, 1973; Supporting Information 2) of P and S
185 arrival times. An optimal damping factor is estimated using trade-off curves (Supporting
186 Information 1) of residual and model variance, the latter being defined using the
187 “roughness” parameter of Greenfield et al. (2016). The preferred model is obtained after
188 16 iterations showing an overall RMS of 0.25 s and a variance of 0.15 s. and residuals (see
189 Supporting Information 3). These values represent a decrease of about 37% in RMS and
190 45% in variance compared to those from the initial model. Final hypocenters have average
191 arrival time residuals of 0.13 s and 0.79 s for P- and S-wave onsets, respectively. Location
192 uncertainties estimated from marginal probability density functions are on the order of 6
193 km, 5 km, and 8 km for the east, north and depth coordinates, respectively.

194

195 *Model Resolution*

196 Based on the results of numerous previous LET investigations, the distribution of events
197 and stations in this study would lead one to expect an overall spatial resolution of
198 structure on the order of tens of km. Nevertheless, the irregular distribution of both
199 stations and earthquakes and the highly nonlinear nature of the inverse problem requires
200 that we document how resolution varies within the model volume. Two common ways to
201 assess the resolution of seismic velocity models are the checkerboard test (e.g., Spakman
202 and Nolet, 1988) and bootstrap resampling (e.g., Calvert et al., 2000; Hicks et al., 2014;
203 León-Ríos et al., 2021). In both cases, synthetic data are calculated in hypothetical models
204 with different sizes and shapes of velocity anomalies. Random noise based on the
205 standard deviation is typically added to the synthetic data to simulate actual data quality
206 (e.g., Hicks et al., 2014; Comte et al., 2019). These synthetic datasets are then inverted
207 following the same procedure as that for the real data and a comparison between the
208 actual and recovered models is made to evaluate resolution scale lengths.

209 *Checkerboard test*

210 The checkerboard resolution tests assumed equi-dimensional anomalies of 15 km, 20 km
211 and 30 km length scale, within which velocities were perturbed by $\pm 5\%$ to form a
212 checkerboard pattern (Supporting Information 4 and 5). Gaussian noise of $1/3 \sigma$ of arrival
213 time was added to the synthetic data at a level commensurate with the anticipated
214 uncertainties in the observations, and the result was inverted following the same
215 procedure as that for the actual model. The results for the 15 km dimension anomaly
216 (Supporting Information 4 and 5) show that it is possible to recover the initial
217 perturbations in much of the model volume at this scale. In general, we infer that the
218 data is capable of recovering wavespeed variations at this scale down to 150 km with a
219 geometry consistent with the shape of the subduction margin. Tests performed with
220 smaller dimension perturbations indicate that 15 km anomalies are the smallest size for
221 interpreting possible geological structures.

222

223 *Bootstrap resampling*

224 The bootstrapping technique is useful to assess the sensitivity of seismic velocity models
225 with respect to the completeness of the event catalog. The bootstrap resampling method
226 suggests that event-based resampling should produce similar results to resampling
227 individual picks (e.g., Calvert et al., 2000; Hicks et al., 2014). We randomly selected 80% of
228 the events in the original data and inverted following the same procedure as for the actual
229 models. Resulting V_p , V_s and V_p/V_s seismic velocity models (see Supporting Information
230 6) recover most of the anomalies observed in the actual models indicating that the results
231 are insensitive to the event selection criteria. Uncertainties estimated from the
232 bootstrapped resampling are about ± 0.025 km/s for V_p and V_s and about ± 0.004 for
233 V_p/V_s .

234

235 **4. Results**

236 *Hypocenter catalog*

237 The catalog of well constrained locations has 16,349 events with an average location
238 uncertainty of 6.90 km. Most of the events with depths between 30 km to 120 km depth
239 are located along the subduction interface (slab 2.0, Hayes et al., 2018; Figure 2). Shallow
240 seismicity (<10 km) is associated with the location of mining operations (Figure 2).
241 Earthquakes in the northern part of the model (cross sections P1-P4) are predominantly
242 intermediate-depth (80 km - 120 km depth), while those in the south (cross-sections P5-
243 P8) are more evenly distributed along the plate interface. The northernmost sections (P1
244 and P2) include upper crustal seismicity that correlates spatially with both the Atacama
245 and Domeyko fault systems, consistent with the active nature of these large-scale systems
246 (Comte et al., 2002b; Bloch et al., 2014; Sippl et al., 2018; 2023). Section P2 also shows a
247 cluster of seismicity at the coast located within the Nazca plate at ~ 40 km depth that is
248 consistent with the Michilla cluster identified in previous catalogues from Fuenzalida et al.
249 (2013) and Pasten-Araya et al. (2021) after the 2007 Tocopilla earthquake. At greater
250 depths ($\sim 80 - 110$ km), clusters of seismicity (C1 in Figure 2) are found within the Nazca

251 plate. An additional dense cluster of seismicity evident in section P4 (Figure 2)
252 corresponds to the Jujuy seismic nest (Valenzuela-Malebran et al. 2022). We observe
253 seismicity at shallower depths (<50 km) in section P5 at a distance of ~400 km from the
254 trench that might be related to volcanic activity from either the Lazufre magmatic body or
255 the Altiplano-Puna magmatic body (Ward et al., 2014; 2017). Sections P6 and P7 show
256 offshore clustered seismicity with an NNW trend and a west dipping alignment that
257 reaches down to the plate interface which is consistent with the observations from
258 Gonzalez-Vidal et al. (2023). Similar NNW seismicity lineaments are observed to the north
259 (from profile P4 to P6, Figure 2), which suggests a regional structural pattern in this
260 segment of the margin. In fact, these kinds of seismicity lineaments were previously
261 observed further north by Pasten-Araya et al. (2021), who identified an active offshore
262 splay fault off the coast of Antofagasta. The observed shallow seismicity in profiles P4-P7
263 suggests a similar active structure to the south of 24°S.

264

265 *Seismic tomography*

266 First order structures observed in the tomographic models (Figure 3, 4, S7 and S8) include
267 the Nazca plate imaged to depths of ~100 km with an east dipping anomaly with $V_p \sim 7.0 -$
268 8.0 km/s and $V_s \sim 4.0 - 4.5$ km/s. The South American plate shows V_p values of $\sim 5.0 - 7.0$
269 km/s and $V_s \sim 3.0 - 4.0$ km/s which are consistent with those found in previous
270 investigations (Husen et al., 2000; Haberland and Rietbrock, 2001; Schurr et al., 2006;
271 Pasten-Araya et al., 2021). The average value of V_p/V_s determined with the Wadati
272 diagram (Wadati et al., 1933; $V_p/V_s = 1.77$) is retained in the inversion. We observe a
273 heterogeneous distribution of anomalies in the whole segment with several transition
274 areas from high ($V_p/V_s > 1.80$) to low ($V_p/V_s < 1.80$) ratios observed in both lower and
275 upper plate (Figure 3 and 4). These anomalies and transition areas can be correlated with
276 geological structures observed at the surface, such as the AFS, DFS, the Salar de Atacama,
277 and the Salar Punta Negra (see section $z = 10$ km in Figure 4).

278 In a closer view of the continental crust, section P1 (Figure 3) shows a heterogeneous
279 velocity structure with $V_p \sim 6.0$ km/s in the first 10 km depth and between 6.0 -7.0 km/s at
280 10 – 30 km depth. The V_p/V_s model shows an anomaly (>1.80 ; labeled A1 in Figure 4)
281 located at the coastline in the upper crust. Eastward, the model shows a low V_p/V_s patch
282 (<1.74 ; labeled A2 in Figure 4), that extends along the whole segment at $\sim 69^\circ\text{W}$ from near
283 the surface to 30 km depth (Figure 4). In section P2 the upper crust shows a more
284 heterogeneous forearc between 200 – 300 km from the trench with $V_p \sim 6.5$ down to 30
285 km depth and alternating patches with low and high V_p/V_s regions. In particular, the
286 V_p/V_s model illuminates a large high ratio (>1.82) anomaly located at shallow depths
287 which is coincident with the location of the Salar de Atacama. The model also shows
288 transitions from high (>1.80) to low (<1.75) V_p/V_s ratios highlighting the heterogeneity of
289 the segment across the forearc. Continuing to the south, sections P3 to P6 for V_p/V_s show
290 two large patches (A2, A5) with low ratios (<1.75) which are contoured by sub-vertical
291 elongated anomalies ($V_p/V_s > 1.77$) that reach down to the interplate interface. Another
292 unusual vertical-elongated feature appears at $24^\circ\text{-}24.5^\circ\text{S}$, in section P4 and P5, below the
293 Cordillera de los Andes. This anomaly (A6), with $V_p/V_s \sim 1.80$, is accompanied by shallow
294 seismicity and is coincident with a low resistivity feature identified by other geophysical
295 studies in the area (Diaz et al., 2012; Araya-Vargas et al., 2019).

296 In the region of the mantle wedge, interplate boundary and subducted plate, P1 shows an
297 area of $V_p \sim 8.0$ km/s close to the plate interface at 50 km depth that locates above a
298 cluster of seismicity within the Nazca plate. At greater depths ($>80 - 100$ km), we observe
299 a large (150 km width x 40 km depth) low V_p/V_s (<1.80 ; labeled A3 in Figure 4) which
300 correlates with the clustered seismicity within the oceanic crust. In section P2, the 8.0
301 km/s V_p east-dipping-contour shifts upwards in comparison to P1. In this section, at
302 distances >300 km from the trench and at $\sim 50\text{-}70$ km depth, we find areas with V_p values
303 $> 7.6\text{-}7.8$ km/s that illuminate the mantle wedge that are consistent with values suggested
304 by Comte et al. (2023). In sections P3 to P6, V_p in the lower part of the oceanic plate has a
305 value of 8.2 km/s (labeled A4 in Figure 4). The oceanic slab here has V_p/V_s ratios > 1.82 ,
306 distinguishing it from the slab in the northern profiles. Sections P6, P7 and P8 show a

307 westward shift of the mantle wedge marked by the $V_p \sim 7.6-7.8$ km/s contours at a
308 distance about 300 km from the trench. V_p/V_s in the vicinity of the Taltal ridge in sections
309 P6 and P7 (labeled A7 in Figure 4) is low (<1.76). A similar feature, along with the
310 surrounding seismicity, has been described for subducted seamounts in Ecuador (Carnegie
311 ridge; Leon-Rios et al., 2021) and Costa Rica (Husen et al., 2002). Finally, sections P7 and
312 P8 show a large high (>1.80) V_p/V_s anomaly (labeled A8 in Figure 4) that extends for about
313 100 km in the upper crust.

314

315 **5. Interpretation and Discussion**

316 *Seismic distribution and first-order structures*

317 Our derived 3D V_p , V_s and V_p/V_s velocity models show the structure of the subducting
318 Nazca plate down to 200 km depth (Figure 3 and 4). The upper continental crust has
319 seismic velocities $V_p \sim 5.0 - 7.0$ km/s and $V_s \sim 3.0 - 4.0$ km/s. The continental Moho
320 discontinuity associated with $V_p \sim 7.7$ km/s implies a crustal thickness of the South
321 American plate of around 40 – 50 km below the forearc, which is consistent with previous
322 observations (e.g., Husen et al., 2000; Haberland et al., 2001). At a distance of 300 km east
323 of the trench and at depths $> \sim 50$ km, we observe the mantle wedge in most of the
324 profiles (see Figure 3).

325 Below the coastal area, the seismicity shows several clusters that could be associated with
326 regional structural features of the upper and lower plate. Southward from the Mejillones
327 Peninsula (P4 to P8, Figure 3 and 4) the seismicity appears to be distributed in lineaments
328 (L1, L2, L3) striking northwest, in concordance with structures observed onshore in the
329 upper plate (Figure 1; Mavor et al. 2020, and references therein), while to the north the
330 seismicity presents a more heterogenous distribution. This change could reflect a
331 latitudinal segmentation of the active structures near the interplate boundary, at least
332 when considering the coverage of our relocated catalog. In particular, P6 and P7 show
333 dense clusters of seismicity offshore, which suggest the presence of west- and east-

334 vergent structures that could be influenced by the Taltal ridge subduction and/or the
335 obliquity of the AFS in the area (Mavor et al. 2020).

336 At greater depths, we observe two prominent features in the seismicity distribution: (1)
337 intense seismic activity at ~100 km depth that coincides with a low Vp/Vs region (labeled
338 A3 in Figure 4) which collocates with the subducting Nazca plate (P1 to P3 in Figure 3). We
339 note that previous studies have identified Vp/Vs ratios with similar values (Herrera et al.,
340 2018). These reduced Vp/Vs values suggest a more rigid and dehydrated slab prone to a
341 localized increase in intermediate-depth seismic activity. (2) We observe seismic activity at
342 depths between 150 km – 200 km, located mostly at the northern profiles (sections P1-
343 P4). P4 highlights the compressive Jujuy seismic nest (Valenzuela-Malebran et al., 2022).
344 Compared with the Slab2 model (Hayes et al., 2018), our seismic catalog suggests a larger
345 dip of the subducting Nazca plate at depths between 150 km - 200 km in the northern
346 profiles (P1-P4).

347 *Large-scale upper-crust features*

348 The continental crust shows a sequence of low and high Vp/Vs anomalies (Figure 3b).
349 Along the coastal area, and correlating with the AFS, most of the profiles show high Vp/Vs
350 values that could be associated with a more fractured crust due to this fracture zone. This
351 correlation is particularly evident northward of ~25°S (Figure 4). In contrast, the coastal
352 area in the zone of the Taltal ridge subduction is characterized by low Vp/Vs values which
353 could be explained as a change in fluid transport inside the crust above this subducted
354 feature. Coincidentally, the structures associated with the AFS show local rotations in this
355 zone (Figure 4). In a similar way, at distances of ~200 km – 250 km from the trench (Figure
356 3b), we observe another high Vp/Vs zone that coincides with the DFS. We infer that, in
357 most profiles (Figure 3 and 4), this large-scale, seismically active geological structure
358 extends down to ~50 km depth and is associated with the large porphyry copper deposits
359 in the region (Reutter et al., 1996; Tomlinson and Blanco, 1997a; 1997b; Camus and
360 Dilles, 2001). Eastward from the DFS, low Vp/Vs anomalies (A1-A4, <1.80; Figure 3 and 4)
361 may be associated with an ancient magmatic arc that might have metamorphosed the

362 surrounding area (e.g. Diaz et al., 2012) and contributed to the accumulation of porphyry
363 copper deposits (Comte et al., 2023; Chen and Wu, 2020). This observation coincides with
364 the location of large copper mining operations in the area such as Chuquicamata, Gabriela
365 Mistral and Escondida, and suggests that LET technique can be used as a tool to identify
366 and characterize porphyry copper deposits at greater depths. In terms of absolute Vp
367 velocity, and at crustal depths (< 50 km), the DFS is in general correlated with a transition
368 from high Vp to the west to low Vp to the east of this structural limit, which could reflect a
369 west-east thermal gradient related to active magmatic arc and subduction geometry
370 (Contreras-Reyes et al., 2021) and/or the presence of high density basement units related
371 to ancient volcanic arcs westward from the DFS (Bascuñán et al., 2016). The presence of
372 cold and dense basement westward from the DFS is concordant with the more rigid (low
373 Vp/Vs) crust observed between the AFS and DFS (Figures 3 and 4). East of the DFS, Vp/Vs
374 values show a more heterogeneous distribution with higher strength (low Vp/Vs) in the
375 southern portion of the Salar de Atacama basin (SdA) and to the southeast of the Salar de
376 Punta Negra basin (Figure 4). By contrast, higher Vp/Vs anomalies are located to the north
377 of the SdA. This heterogeneous distribution in strength could be related to the variability
378 of the ancient basements in this region (e.g. Niemeyer et al., 2018) and the presence of
379 regional structures, as the northwest Calama-Olacapato-El Toro lineament (COT, Lindsay
380 et al., 2001) that seems to control the strength change between the northern and
381 southern portions of the SdA region (figure 4).

382 At a regional scale, the succession of different strength bands (roughly north-south) in the
383 forearc correlates well with large scale electric resistivity anomalies observed in
384 magnetotellurics studies of the zone (Slezak et al., 2021; Contreras-Reyes et al., 2021),
385 where crustal low strength anomalies (high Vp/Vs) correlate with low resistivity zones
386 associated with costal large-scale structures (the AFS) and the DFS.

387

388 *Subducted slab, Mantle wedge and Fluid circulation*

389 First-order observations (sections P3-P7 in Figure 3) suggest a hydrated slab subducting
390 down to ~80 - 90 km depth. At that point, we observe a transition to lower Vp/Vs (<1.76)
391 suggesting a dehydration process consistent with temperature and pressure at these
392 depths (Haberland and Rietbrock, 2001) which leads to a dryer slab at greater depths
393 (>100 km). As mentioned before, the Vp/Vs model (Figure 3 and 4) shows elevated ratios
394 (>1.77) at shallower depths (5 -10 km) that can be associated with the SdA and Salar Punta
395 Negra basins. Moreover, the high Vp/Vs ratios allow us to estimate the in-depth extent of
396 the fluids circulating down to ~30 km depth. At 30 km depth, we observe a predominantly
397 low Vp/Vs region (<1.77) that covers most of the area of study. However, in profiles P7-P8
398 a high Vp/Vs anomaly (labeled A8 in Figure 4) can be observed. This feature is more
399 prominent at greater depths (~50 km), where we clearly observe a transition to higher
400 values of Vp/Vs (>1.80). We attribute this anomaly to an increase in the fluid circulation
401 promoted by the Taltal ridge, which subducts between 24°S – 25°S. The presence of large-
402 scale, shallow oceanic features can cause basal erosion and fractures in the overriding
403 plate (Scholz and Small, 1997; Contreras-Reyes et al., 2011) enhancing the transport of
404 fluids from deeper to shallower depths (Collot et al., 2004; Marcaillou et al., 2016; Leon-
405 Rios et al., 2021)

406 Finally, profiles P4 and P5 (Figure 3) show an elongated anomaly (labeled A6) with
407 Vp/Vs~1.79 - 1.80 located at 50 km depth and ~ 300 km from the trench. We interpret this
408 feature as fluids moving upwards from the plate interface towards the surface, promoting
409 partial melting and feeding the northern edge of the LMB and other volcanic complexes
410 (Haberland and Rietbrock, 2001; Diaz et al., 2006; 2012; Araya, 2019). The shallow
411 seismicity observed ~400 km from the trench corroborates the hypothesis of fluid
412 circulation in the area. We note that the SdA area (around profile P3-P4, Figure 4)
413 correlates well with a part of the mantle wedge (depth ≥ 50 km) characterized by high Vp
414 (>8.0 km/s) and low Vp/Vs (<1.70) bounded by low Vp (~7.5 km/s) and high Vp/Vs (>1.80),
415 which suggest a correlation between anomalies associated with high fluid content (and
416 high temperatures) and the active volcanism in the area, including the local eastward
417 migration of the volcanic arc around the SdA.

418

419 **Conclusion**

420 Data from ~23,000 earthquakes recorded by a large temporary deployment that operated
421 in northern Chile for an 8-month period allowed us to characterize the seismotectonic
422 structure of the Taltal segment in northern Chile. We applied LET to jointly derive 3D
423 seismic velocity models for V_p , V_s and V_p/V_s and earthquake locations. The seismicity
424 occurs mostly along the slab interface but also within large-scale structures in the
425 overriding plate. At greater depths, we observe a change in the dip of the slab that we
426 suggest results from a strong slab-pull. Offshore, we observe clustered seismicity that we
427 interpret as a splay fault that reaches the slab interface. This seismicity appears to be a
428 consequence of the Taltal ridge subducting in the southern part of the region.

429 The V_p and V_s seismic velocity models illuminate first-order structures such as the oceanic
430 plate and the South American upper-crust. The V_p/V_s model identifies regions which
431 change from reduced (<1.77) to elevated (>1.77) ratios that we interpret as large-scale
432 fault systems that penetrate down to the seismogenic zone. The oceanic slab also shows a
433 transition from elevated (>1.80) to reduced (<1.76) V_p/V_s suggesting a highly hydrated
434 plate at seismogenic depths that dehydrates and evolves into a dryer and more rigid slab
435 at greater depths. The latter might also contribute to explaining the high rate of intraplate
436 seismicity observed at ~200 km depth.

437 Low V_p/V_s anomalies (<1.75) at shallow depths (<20 km) collocate with sites of large
438 copper mining operations and suggests the use of LET to illuminate locations of porphyry
439 copper deposits. High V_p/V_s anomalies (>1.80) at ~50 km depth suggest circulation of
440 fluids caused by the incoming Taltal ridge that erodes and fractures the southern edge of
441 overriding plate. They also suggest the presence of partial melting associated with the
442 Lazufre Magmatic Body and other small volcanic systems.

443

444

445

446

447

448

449

450

451 **Acknowledgments**

452 The authors acknowledge the funding from Fondecyt Postdoctorado 2022, No 322099;
453 NSF-China-ANID PI18003; PIA AFB220002. Alejandro Faundez and Gerardo Peña who
454 assisted in the network deployment. Section profiles and map view figures were made
455 using GMTv5 (Wessel et al., 2013) and colored following the guidelines for CVD
456 accessibility by Cramer et al. (2020).

457 **Data availability**

458 Temporary network details in FDSN database (Andreas Rietbrock, Diana Comte, & Sergio
459 Leon-Rios (2020): Taltal temporary deployment. International Federation of Digital
460 Seismograph Networks. Dataset/Seismic Network. <https://doi.org/10.7914/mc8r-ft72>).

461 Initial and final models as well as hypocenter catalog, arrival times are available in
462 ZENODO with the DOI 10.5281/zenodo.8271327.

463

464 **References**

- 465 1. Abe, K. (1979). Size of great earthquakes of 1837–1974 inferred from tsunami data.
466 *Journal of Geophysical Research: Solid Earth*, 84(B4), 1561-1568.
- 467 2. Aki, K., & Lee, W. H. K. (1976). Determination of three-dimensional velocity anomalies
468 under a seismic array using first P arrival times from local earthquakes: 1. A
469 homogeneous initial model. *Journal of Geophysical research*, 81(23), 4381-4399.

- 470 3. Aki, K., Christoffersson, A., & Husebye, E. S. (1977). Determination of the three-
471 dimensional seismic structure of the lithosphere. *Journal of Geophysical Research*,
472 82(2), 277-296.
- 473 4. Angermann, D., Klotz, J., & Reigber, C. (1999). Space-geodetic estimation of the
474 Nazca-South America Euler vector. *Earth and Planetary Science Letters*, 171(3), 329-
475 334.
- 476 5. Arabasz Jr, W. J. (1971). Geological and geophysical studies of the Atacama fault zone
477 in northern Chile. Doctoral dissertation, California Institute of Technology.
- 478 6. Arabasz, W. J. (1968). Geologic structure of the Taltal Area, Northern Chile, in relation
479 to the earthquake of December 28, 1966. *Bulletin of the Seismological Society of*
480 *America*, 58(3), 835-842.
- 481 7. Araya Vargas, J., Meqbel, N. M., Ritter, O., Brasse, H., Weckmann, U., Yáñez, G., &
482 Godoy, B. (2019). Fluid distribution in the Central Andes subduction zone imaged with
483 magnetotellurics. *Journal of Geophysical Research: Solid Earth*, 124(4), 4017-4034.
- 484 8. Barrientos, S. (2018). The seismic network of Chile. *Seismological Research Letters*,
485 89(2A), 467-474.
- 486 9. Bascuñán, S., Arriagada, C., Le Roux, J., Deckart, K., 2016. Unraveling the Peruvian
487 Phase of the Central Andes: Stratigraphy, sedimentology and geochronology of the
488 Salar de Atacama Basin (22°30-23°S), northern Chile. *Basin Res.* 28, 365–392.
489 <https://doi.org/10.1111/bre.12114>
- 490 10. Beck, S., Barrientos, S., Kausel, E., & Reyes, M. (1998). Source characteristics of
491 historic earthquakes along the central Chile subduction Askew et Alzone. *Journal of*
492 *South American Earth Sciences*, 11(2), 115-129.
- 493 11. Béjar-Pizarro, M., Carrizo, D., Socquet, A., Armijo, R., Barrientos, S., Bondoux, F., ... &
494 Vigny, C. (2010). Asperities and barriers on the seismogenic zone in North Chile: state-
495 of-the-art after the 2007 M w 7.7 Tocopilla earthquake inferred by GPS and InSAR
496 data. *Geophysical Journal International*, 183(1), 390-406.

- 497 12. Brocher, T. M. (2005). Empirical relations between elastic wavespeeds and density in
498 the Earth's crust. *Bulletin of the seismological Society of America*, 95(6), 2081-2092.
- 499 13. Calle-Gardella, D., Comte, D., Farías, M., Roecker, S., & Rietbrock, A. (2021). Three-
500 dimensional local earthquake tomography of pre-Cenozoic structures in the coastal
501 margin of central Chile: Pichilemu fault system. *Journal of Seismology*, 25(2), 521-533.
- 502 14. Calvert, A., Sandvol, E., Seber, D., Barazangi, M., Roecker, S., Mourabit, T., ... & Jabour,
503 N. (2000). Geodynamic evolution of the lithosphere and upper mantle beneath the
504 Alboran region of the western Mediterranean: Constraints from travel time
505 tomography. *Journal of Geophysical Research: Solid Earth*, 105(B5), 10871-10898.
- 506 15. Camus, F., & Dilles, J. H. (2001). A special issue devoted to porphyry copper deposits
507 of northern Chile. *Economic Geology*, 96(2), 233-237.
- 508 16. Cembrano, J., González, G., Arancibia, G., Ahumada, I., Olivares, V., & Herrera, V.
509 (2005). Fault zone development and strain partitioning in an extensional strike-slip
510 duplex: A case study from the Mesozoic Atacama fault system, Northern Chile.
511 *Tectonophysics*, 400(1-4), 105-125.
- 512 17. Chen, H., & Wu, C. (2020). Metallogensis and major challenges of porphyry copper
513 systems above subduction zones. *Science China Earth Sciences*, 63, 899-918.
- 514 18. Chlieh, M., De Chabalier, J. B., Ruegg, J. C., Armijo, R., Dmowska, R., Campos, J., &
515 Feigl, K. L. (2004). Crustal deformation and fault slip during the seismic cycle in the
516 North Chile subduction zone, from GPS and InSAR observations. *Geophysical Journal
517 International*, 158(2), 695-711.
- 518 19. Christensen, N. I. (1996). Poisson's ratio and crustal seismology. *Journal of
519 Geophysical Research: Solid Earth*, 101(B2), 3139-3156.
- 520 20. Collot, J. Y., Marcaillou, B., Sage, F., Michaud, F., Agudelo, W., Charvis, P., ... & Spence,
521 G. (2004). Are rupture zone limits of great subduction earthquakes controlled by
522 upper plate structures? Evidence from multichannel seismic reflection data acquired

- 523 across the northern Ecuador–southwest Colombia margin. *Journal of Geophysical*
524 *Research: Solid Earth*, 109(B11).
- 525 21. Comte, D., & Pardo, M. (1991). Reappraisal of great historical earthquakes in the
526 northern Chile and southern Peru seismic gaps. *Natural hazards*, 4(1), 23-44.
- 527 22. Comte, D., Carrizo, D., Roecker, S., Ortega-Culaciati, F., & Peyrat, S. (2016). Three-
528 dimensional elastic wave speeds in the northern Chile subduction zone: variations in
529 hydration in the supraslab mantle. *Geophysical Supplements to the Monthly Notices*
530 *of the Royal Astronomical Society*, 207(2), 1080-1105.
- 531 23. Comte, D., Farías, M., Calle-Gardella, D., Navarro-Aranguiz, A., Roecker, S., &
532 Rietbrock, A. (2023). Anomalous intraslab structure revealed by the analysis of
533 aftershocks of the Mw 6.7 Coquimbo-La Serena earthquake of 20 January 2019.
534 *Tectonophysics*, 846, 229660.
- 535 24. Comte, D., Farias, M., Roecker, S., & Russo, R. (2019). The nature of the subduction
536 wedge in an erosive margin: Insights from the analysis of aftershocks of the 2015 Mw
537 8.3 Illapel earthquake beneath the Chilean Coastal Range. *Earth and Planetary Science*
538 *Letters*, 520, 50-62.
- 539 25. Comte, D., Haessler, H., Dorbath, L., Pardo, M., Monfret, T., Lavenu, A., ... & Hello, Y.
540 (2002). Seismicity and stress distribution in the Copiapo, northern Chile subduction
541 zone using combined on-and off-shore seismic observations. *Physics of the earth and*
542 *planetary interiors*, 132(1-3), 197-217.
- 543 26. Comte, D., Palma, G., Vargas, J. *et al.* Imaging the subsurface architecture in porphyry
544 copper deposits using local earthquake tomography. *Sci Rep* **13**, 6812 (2023).
545 <https://doi.org/10.1038/s41598-023-33820-w>
- 546 27. Contreras-Reyes, E., & Carrizo, D. (2011). Control of high oceanic features and
547 subduction channel on earthquake ruptures along the Chile–Peru subduction zone.
548 *Physics of the Earth and Planetary Interiors*, 186(1-2), 49-58.

- 549 28. Cooke, D. R., Hollings, P., & Walshe, J. L. (2005). Giant porphyry deposits:
550 characteristics, distribution, and tectonic controls. *Economic geology*, 100(5), 801-
551 818.
- 552 29. Cramer, F., Shephard, G. E., & Heron, P. J. (2020). The misuse of colour in science
553 communication. *Nature communications*, 11(1), 1-10.
- 554 30. de Ballore, F. D. M. (1913, January). Historia sísmica de los andes meridionales al sur
555 del paralelo XVI. In *Anales de la Universidad de Chile* (No. 71, pp. 87-129).
- 556 31. Delouis, B., Pardo, M., Legrand, D., & Monfret, T. (2009). The M_w 7.7 Tocopilla
557 earthquake of 14 November 2007 at the southern edge of the northern Chile seismic
558 gap: Rupture in the deep part of the coupled plate interface. *Bulletin of the*
559 *Seismological Society of America*, 99(1), 87-94.
- 560 32. Delph, J. R., Ward, K. M., Zandt, G., Ducea, M. N., & Beck, S. L. (2017). Imaging a
561 magma plumbing system from MASH zone to magma reservoir. *Earth and Planetary*
562 *Science Letters*, 457, 313-324.
- 563 33. DeMets, C., Gordon, R. G., Argus, D. F., & Stein, S. (1990). Current plate motions.
564 *Geophysical journal international*, 101(2), 425-478.
- 565 34. DeMets, C., Gordon, R. G., Argus, D. F., & Stein, S. (1994). Effect of recent revisions to
566 the geomagnetic reversal time scale on estimates of current plate motions.
567 *Geophysical research letters*, 21(20), 2191-2194.
- 568 35. Deschamps, A., H. Lyon-Caen, and R. Madariaga (1980). Etude du tremblement de
569 terre de Taltal (Chili 1966) à partir des ondes sismiques de longue période. *Ann.*
570 *Geophys*, 36(2),
- 571 36. Díaz, D., Brasse, H., & Ticona, F. (2012). Conductivity distribution beneath Lascar
572 volcano (Northern Chile) and the Puna, inferred from magnetotelluric data. *Journal of*
573 *Volcanology and Geothermal Research*, 217, 21-29.
- 574 37. GeoForschungsZentrum, D. (2006). IPOC Seismic Network.

- 575 38. González-Vidal, D., Moreno, M., Sippl, C., Baez, J. C., Ortega-Culaciati, F. H., Lange, D.,
576 ... & Araya, R. (2023). Relation between oceanic plate structure, patterns of interplate
577 locking and microseismicity in the 1922 Atacama Seismic Gap. *Authorea Preprints*.
- 578 39. Götze, H. J., & Krause, S. (2002). The Central Andean gravity high, a relic of an old
579 subduction complex?. *Journal of South American Earth Sciences*, 14(8), 799-811.
- 580 40. Götze, H. J., Lahmeyer, B., Schmidt, S., Strunk, S., & Araneda, M. (1990). Central Andes
581 gravity data base. *Eos, Transactions American Geophysical Union*, 71(16), 401-407.
- 582 41. Greenfield, T., White, R. S., & Roecker, S. (2016). The magmatic plumbing system of
583 the Askja central volcano, Iceland, as imaged by seismic tomography. *Journal of*
584 *Geophysical Research: Solid Earth*, 121(10), 7211-7229.
- 585 42. Haberland, C., & Rietbrock, A. (2001). Attenuation tomography in the western central
586 Andes: A detailed insight into the structure of a magmatic arc. *Journal of Geophysical*
587 *Research: Solid Earth*, 106(B6), 11151-11167.
- 588 43. Hacker, B. R., Abers, G. A., & Peacock, S. M. (2003a). Subduction factory 1. Theoretical
589 mineralogy, densities, seismic wave speeds, and H₂O contents. *Journal of Geophysical*
590 *Research: Solid Earth*, 108(B1).
- 591 44. Hacker, B. R., Peacock, S. M., Abers, G. A., & Holloway, S. D. (2003b). Subduction
592 factory 2. Are intermediate-depth earthquakes in subducting slabs linked to
593 metamorphic dehydration reactions?. *Journal of Geophysical Research: Solid Earth*,
594 108(B1).
- 595 45. Hayes, G. P., Moore, G. L., Portner, D. E., Hearne, M., Flamme, H., Furtney, M., &
596 Smoczyk, G. M. (2018). Slab2, a comprehensive subduction zone geometry model.
597 *Science*, 362(6410), 58-61.
- 598 46. Herrera, C., Pastén-Araya, F., Cabrera, L., Potin, B., Rivera, E., Ruiz, S., ... & Contreras-
599 Reyes, E. (2023). Rupture properties of the 2020 M_w 6.8 Calama (northern Chile)
600 intraslab earthquake. Comparison with similar intraslab events in the region.
601 *Geophysical Journal International*, 232(3), 2070-2079.

- 602 47. Hicks, S. P., Rietbrock, A., Ryder, I. M., Lee, C. S., & Miller, M. (2014). Anatomy of a
603 megathrust: The 2010 M8.8 Maule, Chile earthquake rupture zone imaged using
604 seismic tomography. *Earth and Planetary Science Letters*, 405, 142-155.
- 605 48. Holtkamp, S. G., Pritchard, M. E., & Lohman, R. B. (2011). Earthquake swarms in South
606 America. *Geophysical Journal International*, 187(1), 128-146.
- 607 49. Husen, S., Kissling, E., & Flueh, E. R. (2000). Local earthquake tomography of shallow
608 subduction in north Chile: A combined onshore and offshore study. *Journal of*
609 *Geophysical Research: Solid Earth*, 105(B12), 28183-28198.
- 610 50. Husen, S., Kissling, E., & Quintero, R. (2002). Tomographic evidence for a subducted
611 seamount beneath the Gulf of Nicoya, Costa Rica: The cause of the 1990 Mw= 7.0 Gulf
612 of Nicoya earthquake. *Geophysical Research Letters*, 29(8), 79-1.
- 613 51. Kanamori, H., Rivera, L., Ye, L., Lay, T., Murotani, S., & Tsumura, K. (2019). New
614 constraints on the 1922 Atacama, Chile, earthquake from historical seismograms.
615 *Geophysical Journal International*, 219(1), 645-661.
- 616 52. Kato, A., & Nakagawa, S. (2014). Multiple slow-slip events during a foreshock
617 sequence of the 2014 Iquique, Chile Mw 8.1 earthquake. *Geophysical Research*
618 *Letters*, 41(15), 5420-5427.
- 619 53. Kausel, E., & Campos, J. (1992). The Ms= 8 tensional earthquake of 9 December 1950
620 of northern Chile and its relation to the seismic potential of the region. *Physics of the*
621 *earth and planetary interiors*, 72(3-4), 220-235.
- 622 54. Kelleher, J. A. (1972). Rupture zones of large South American earthquakes and some
623 predictions. *Journal of Geophysical Research*, 77(11), 2087-2103.
- 624 55. Kisslinger, C., & Engdahl, E. R. (1973). The interpretation of the Wadati diagram with
625 relaxed assumptions. *Bulletin of the Seismological Society of America*, 63(5), 1723-
626 1736.

- 627 56. Klein, E., Metois, M., Meneses, G., Vigny, C., & Delorme, A. (2018). Bridging the gap
628 between North and Central Chile: insight from new GPS data on coupling complexities
629 and the Andean sliver motion. *Geophysical Journal International*, 213(3), 1924-1933.
- 630 57. Köther, N., Götze, H. J., Gutknecht, B. D., Jahr, T., Jentzsch, G., Lücke, O. H., ... &
631 Zeumann, S. (2012). The seismically active Andean and Central American margins: Can
632 satellite gravity map lithospheric structures?. *Journal of Geodynamics*, 59, 207-218.
- 633 58. Kühn, C., Brasse, H., & Schwarz, G. (2018). Three-dimensional electrical resistivity
634 image of the volcanic arc in Northern Chile—an appraisal of early magnetotelluric
635 data. *Pure and Applied Geophysics*, 175(6), 2153-2165.
- 636 59. Kushnir, A. F., Lapshin, V. M., Pinsky, V. I., & Fyen, J. (1990). Statistically optimal event
637 detection using small array data. *Bulletin of the seismological society of america*,
638 80(6B), 1934-1950.
- 639 60. Legrand, D., Delouis, B., Dorbath, L., David, C., Campos, J., Marquez, L., ... & Comte, D.
640 (2007). Source parameters of the Mw= 6.3 Aroma crustal earthquake of July 24, 2001
641 (northern Chile), and its aftershock sequence. *Journal of south American earth
642 sciences*, 24(1), 58-68.
- 643 61. León-Ríos, S., Bie, L., Agurto-Detzel, H., Rietbrock, A., Galve, A., Alvarado, A., ... &
644 Woollam, J. (2021). 3D local earthquake tomography of the Ecuadorian margin in the
645 source area of the 2016 Mw 7.8 Pedernales earthquake. *Journal of Geophysical
646 Research: Solid Earth*, 126(3), e2020JB020701.
- 647 62. Lindsay, J. M., de Silva, S., Trumbull, R., Emmermann, R., & Wemmer, K. (2001). La
648 Pacana caldera, N. Chile: a re-evaluation of the stratigraphy and volcanology of one of
649 the world's largest resurgent calderas. *Journal of Volcanology and Geothermal
650 Research*, 106(1), 145–173. [https://doi.org/https://doi.org/10.1016/S0377-
651 0273\(00\)00270-5](https://doi.org/https://doi.org/10.1016/S0377-0273(00)00270-5)
- 652 63. Maksymowicz, A. (2015). The geometry of the Chilean continental wedge: Tectonic
653 segmentation of subduction processes off Chile. *Tectonophysics*, 659, 183-196.

- 654 64. Marcaillou, B., Collot, J. Y., Ribodetti, A., d'Acremont, E., Mahamat, A. A., & Alvarado,
655 A. (2016). Seamount subduction at the North-Ecuadorian convergent margin: Effects
656 on structures, inter-seismic coupling and seismogenesis. *Earth and Planetary Science
657 Letters*, 433, 146-158.
- 658 65. Mavor, S. P., Singleton, J. S., Gomila, R., Heuser, G., Seymour, N. M., Williams, S. A., ...
659 & Stockli, D. F. (2020). Timing, kinematics, and displacement of the Taltal fault system,
660 northern Chile: Implications for the Cretaceous tectonic evolution of the Andean
661 margin. *Tectonics*, 39(2), e2019TC005832.
- 662 66. Meng, L., Huang, H., Bürgmann, R., Ampuero, J. P., & Strader, A. (2015). Dual
663 megathrust slip behaviors of the 2014 Iquique earthquake sequence. *Earth and
664 Planetary Science Letters*, 411, 177-187.
- 665 67. Metois, M., Socquet, A., Vigny, C., Carrizo, D., Peyrat, S., Delorme, A., ... & Ortega, I.
666 (2013). Revisiting the North Chile seismic gap segmentation using GPS-derived
667 interseismic coupling. *Geophysical Journal International*, 194(3), 1283-1294.
- 668 68. Metois, M., Vigny, C., & Socquet, A. (2016). Interseismic coupling, megathrust
669 earthquakes and seismic swarms along the Chilean subduction zone (38–18 S). *Pure
670 and Applied Geophysics*, 173(5), 1431-1449.
- 671 69. Mitchell, M. A., White, R. S., Roecker, S., & Greenfield, T. (2013). Tomographic image
672 of melt storage beneath Askja Volcano, Iceland using local microseismicity.
673 *Geophysical Research Letters*, 40(19), 5040-5046.
- 674 70. Monfret, T., Dorbath, L., Caminade, J. P., Pardo, M., Comte, D., & Ponce, L. (1995). The
675 July 30, Antofagasta earthquake: an “Hypocritical” seismic event. *EOS, Trans. Am.
676 geophys. Un*, 76(46), 427.
- 677 71. Montessus de Ballore F (1912) Historia sísmica de los Andes meridionales al sur del
678 paralelo XVI. Imprenta Cervantes, Santiago, pp 545–591. Delouis, B., Monfret, T.,
679 Dorbath, L., Pardo, M., Rivera, L., Comte, D., ... & Cisternas, A. (1997). The Mw= 8.0

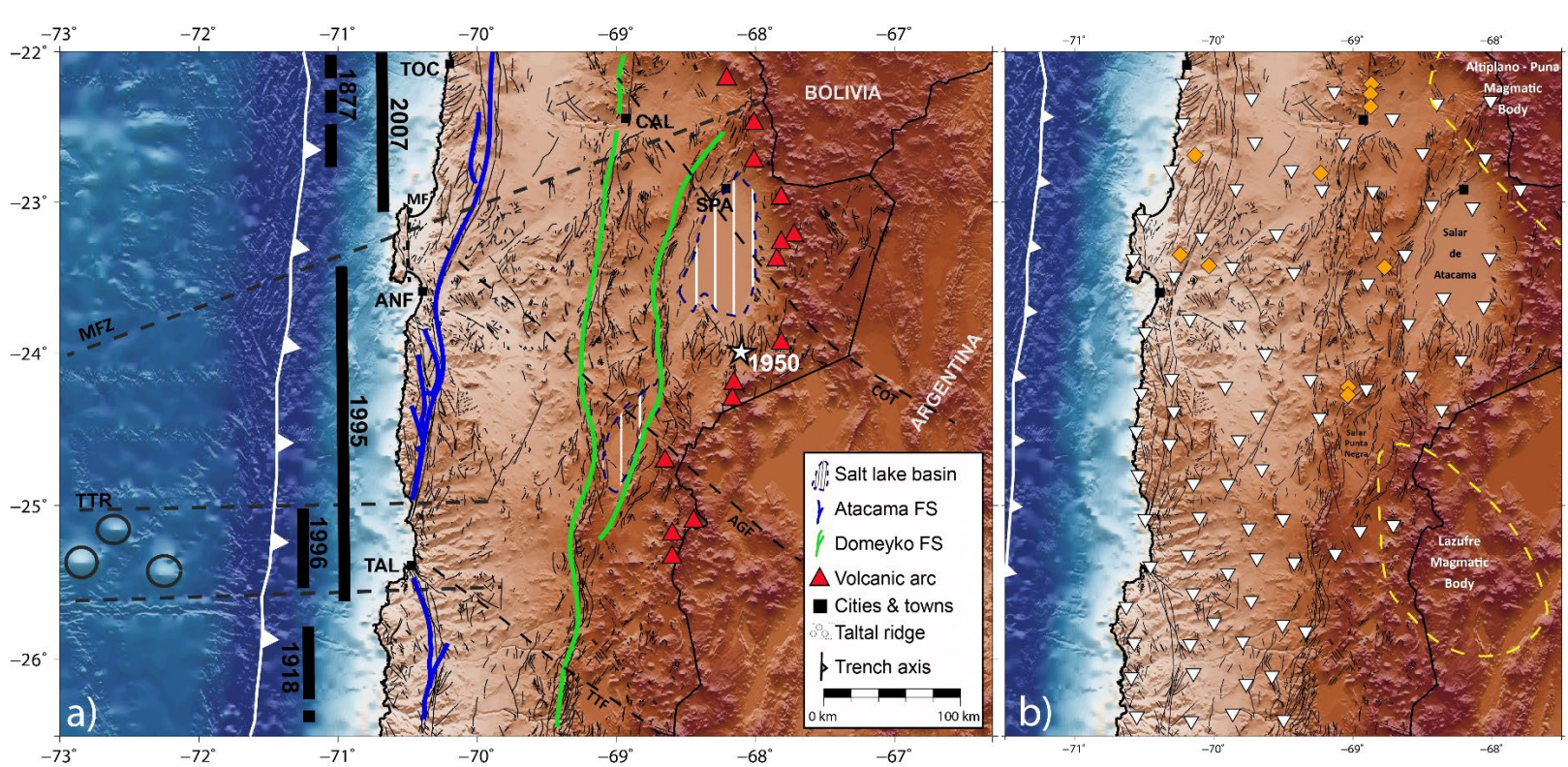
- 680 Antofagasta (northern Chile) earthquake of 30 July 1995: A precursor to the end of
681 the large 1877 gap. *Bulletin of the Seismological Society of America*, 87(2), 427-445.
- 682 72. Niemeyer, H., Götze, J., Sanhueza, M., & Portilla, C. (2018). The Ordovician magmatic
683 arc in the northern Chile-Argentina Andes between 21° and 26° south latitude. *Journal*
684 *of South American Earth Sciences*, 81, 204–214.
685 <https://doi.org/https://doi.org/10.1016/j.jsames.2017.11.016>
- 686 73. Norabuena, E. O., Dixon, T. H., Stein, S., & Harrison, C. G. (1999). Decelerating Nazca-
687 South America and Nazca-Pacific plate motions. *Geophysical Research Letters*, 26(22),
688 3405-3408.
- 689 74. Palacios, C., Ramírez, L. E., Townley, B., Solari, M., & Guerra, N. (2007). The role of the
690 Antofagasta–Calama Lineament in ore deposit deformation in the Andes of northern
691 Chile. *Mineralium Deposita*, 42(3), 301-308.
- 692 75. Pastén-Araya, F., Potin, B., Ruiz, S., Zerbst, L., Aden-Antoniów, F., Azúa, K., ... &
693 Fuenzalida, A. (2021). Seismicity in the upper plate of the Northern Chilean offshore
694 forearc: Evidence of splay fault south of the Mejillones Peninsula. *Tectonophysics*,
695 800, 228706.
- 696 76. Peyrat, S., Madariaga, R., Buforn, E., Campos, J., Asch, G., & Vilotte, J. P. (2010).
697 Kinematic rupture process of the 2007 Tocopilla earthquake and its main aftershocks
698 from teleseismic and strong-motion data. *Geophysical Journal International*, 182(3),
699 1411-1430.
- 700 77. Pisarenko, V. F., Kushnir, A. F., & Savin, I. V. (1987). Statistical adaptive algorithms for
701 estimation of onset moments of seismic phases. *Physics of the earth and planetary*
702 *interiors*, 47, 4-10.
- 703 78. Prévot, R., Roecker, S. W., Isacks, B. L., & Chatelain, J. L. (1991). Mapping of low P
704 wave velocity structures in the subducting plate of the central New Hebrides,
705 southwest Pacific. *Journal of Geophysical Research: Solid Earth*, 96(B12), 19825-
706 19842.

- 707 79. Pritchard, M. E., De Silva, S. L., Michelfelder, G., Zandt, G., McNutt, S. R., Gottsmann,
708 J., ... & Ward, K. M. (2018). Synthesis: PLUTONS: Investigating the relationship
709 between pluton growth and volcanism in the Central Andes. *Geosphere*, 14(3), 954-
710 982.
- 711 80. Rawles, C., & Thurber, C. (2015). A non-parametric method for automatic
712 determination of P-wave and S-wave arrival times: application to local micro
713 earthquakes. *Geophysical Journal International*, 202(2), 1164-1179.
- 714 81. Reutter, K. J., Scheuber, E., & Chong, G. (1996). The Precordilleran fault system of
715 Chuquicamata, northern Chile: Evidence for reversals along arc-parallel strike-slip
716 faults. *Tectonophysics*, 259(1-3), 213-228.
- 717 82. Reutter, K. J., Scheuber, E., & Helmcke, D. (1991). Structural evidence of orogen-
718 parallel strike slip displacements in the Precordillera of northern Chile. *Geologische*
719 *Rundschau*, 80(1), 135-153.
- 720 83. Richards, J. (2016). Clues to hidden copper deposits. *Nature Geoscience*, 9(3), 195-
721 196.
- 722 84. Riller, U., Götze, H. J., Schmidt, S., Trumbull, R. B., Hongn, F., & Petrinovic, I. A. (2006).
723 Upper-crustal structure of the Central Andes inferred from dip curvature analysis of
724 isostatic residual gravity. In *The Andes* (pp. 327-336). Springer, Berlin, Heidelberg.
- 725 85. Roecker, S., Thurber, C., & McPhee, D. (2004). Joint inversion of gravity and arrival
726 time data from Parkfield: New constraints on structure and hypocenter locations near
727 the SAFOD drill site. *Geophysical Research Letters*, 31(12).
- 728 86. Roecker, S., Thurber, C., Roberts, K., & Powell, L. (2006). Refining the image of the San
729 Andreas Fault near Parkfield, California using a finite difference travel time
730 computation technique. *Tectonophysics*, 426(1-2), 189-205.
- 731 87. Ruegg, J. C., Campos, J., Armijo, R., Barrientos, S., Briole, P., Thiele, R., ... & Serrurier,
732 L. (1996). The Mw= 8.1 Antofagasta (North Chile) earthquake of July 30, 1995: first

- 733 results from teleseismic and geodetic data. *Geophysical Research Letters*, 23(9), 917-
734 920.
- 735 88. Ruiz, S., & Madariaga, R. (2018). Historical and recent large megathrust earthquakes
736 in Chile. *Tectonophysics*, 733, 37-56.
- 737 89. Ruiz, S., Metois, M., Fuenzalida, A., Ruiz, J., Leyton, F., Grandin, R., ... & Campos, J.
738 (2014). Intense foreshocks and a slow slip event preceded the 2014 Iquique Mw 8.1
739 earthquake. *Science*, 345(6201), 1165-1169.
- 740 90. Salazar, D., Easton, G., Goff, J., Guendon, J. L., González-Alfaro, J., Andrade, P., ... &
741 Campos, J. (2022). Did a 3800-year-old $M_w \sim 9.5$ earthquake trigger major social
742 disruption in the Atacama Desert?. *Science advances*, 8(14), eabm2996.
- 743 91. Scheuber, E., & Gonzalez, G. (1999). Tectonics of the Jurassic-Early Cretaceous
744 magmatic arc of the north Chilean Coastal Cordillera (22–26 S): A story of crustal
745 deformation along a convergent plate boundary. *Tectonics*, 18(5), 895-910.
- 746 92. Scholz, C. H., & Small, C. (1997). The effect of seamount subduction on seismic
747 coupling. *Geology*, 25(6), 487-490.
- 748 93. Schurr, B., & Rietbrock, A. (2004). Deep seismic structure of the Atacama basin,
749 northern Chile. *Geophysical Research Letters*, 31(12).
- 750 94. Schurr, B., Rietbrock, A., Asch, G., Kind, R., & Oncken, O. (2006). Evidence for
751 lithospheric detachment in the central Andes from local earthquake tomography.
752 *Tectonophysics*, 415(1-4), 203-223.
- 753 95. Sella, G. F., Dixon, T. H., & Mao, A. (2002). REVEL: A model for recent plate velocities
754 from space geodesy. *Journal of Geophysical Research: Solid Earth*, 107(B4), ETG-11.
- 755 96. Sippl, C., Schurr, B., Asch, G., & Kummerow, J. (2018). Seismicity structure of the
756 northern Chile forearc from > 100,000 double-difference relocated hypocenters.
757 *Journal of Geophysical Research: Solid Earth*, 123(5), 4063-4087.

- 758 97. Sippl, C., Schurr, B., Münchmeyer, J., Barrientos, S., & Oncken, O. (2023). The
759 Northern Chile forearc constrained by 15 years of permanent seismic monitoring.
760 *Journal of South American Earth Sciences*, 104326.
- 761 98. Ślęzak, K., Díaz, D., Vargas, J. A., Cordell, D., Reyes-Cordova, F., & Segovia, M. J.
762 (2021). Magnetotelluric image of the Chilean subduction zone in the Salar de Atacama
763 region (23°-24° S): Insights into factors controlling the distribution of volcanic arc
764 magmatism. *Physics of the Earth and Planetary Interiors*, 318, 106765.
- 765 99. Spakman, W., & Nolet, G. (1988). Imaging algorithms, accuracy and resolution in delay
766 time tomography. *Mathematical geophysics: A survey of recent developments in*
767 *seismology and geodynamics*, 155-187.
- 768 100. Tomlinson, A. J., & Blanco, N. (1997a). Structural evolution and displacement history
769 of the west fault systems, Precordillera, Chile, part 1, Post-mineral history, paper
770 presented at VIII Congreso Geológico Chileno. *Soc. Geol. de Chile, Antofagasta, Chile*.
- 771 101. Tomlinson, A. J., & Blanco, N. (1997b). Structural evolution and displacement history
772 of the west fault systems, Precordillera, Chile, part 2, Post-mineral history, paper
773 presented at VIII Congreso Geológico Chileno. *Soc. Geol. de Chile, Antofagasta, Chile*.
- 774 102. Valenzuela-Malebrán, C., Cesca, S., López-Comino, J. A., Zeckra, M., Krüger, F., &
775 Dahm, T. (2022). Source mechanisms and rupture processes of the Jujuy seismic nest,
776 Chile-Argentina border. *Journal of South American Earth Sciences*, 117, 103887.
- 777 103. Victor, P., Oncken, O., & Glodny, J. (2004). Uplift of the western Altiplano plateau:
778 Evidence from the Precordillera between 20 and 21 S (northern Chile). *Tectonics*,
779 23(4).
- 780 104. Victor, P., Sobiesiak, M., Glodny, J., Nielsen, S. N., & Oncken, O. (2011). Long-term
781 persistence of subduction earthquake segment boundaries: Evidence from Mejillones
782 Peninsula, northern Chile. *Journal of Geophysical Research: Solid Earth*, 116(B2).

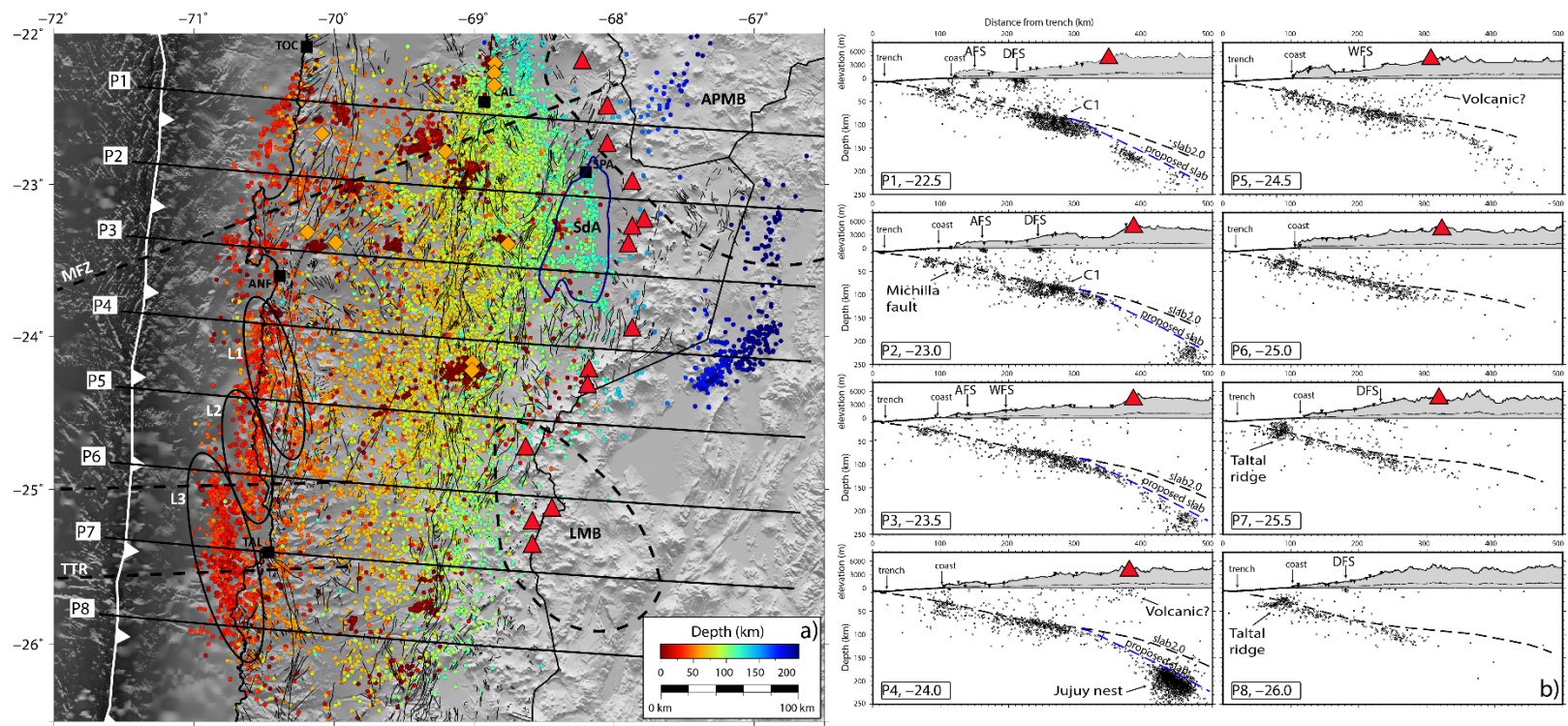
- 783 105. Von Huene, R., Corvalán, J., Flueh, E. R., Hinz, K., Korstgard, J., Ranero, C. R., &
784 Weinrebe, W. (1997). Tectonic control of the subducting Juan Fernández Ridge on the
785 Andean margin near Valparaíso, Chile. *Tectonics*, 16(3), 474-488.
- 786 106. Wadati, K., & Oki, S. (1933). On the travel time of earthquake waves. (Part II). *Journal*
787 *of the Meteorological Society of Japan*. Ser. II, 11(1), 14-28. Ward, K. M., Delph, J. R.,
788 Zandt, G., Beck, S. L., & Ducea, M. N. (2017). Magmatic evolution of a Cordilleran
789 flare-up and its role in the creation of silicic crust. *Scientific reports*, 7(1), 1-8.
- 790 107. Ward, K. M., Delph, J. R., Zandt, G., Beck, S. L., & Ducea, M. N. (2017). Magmatic
791 evolution of a Cordilleran flare-up and its role in the creation of silicic crust. *Scientific*
792 *reports*, 7(1), 9047.
- 793 108. Ward, K. M., Zandt, G., Beck, S. L., Christensen, D. H., & McFarlin, H. (2014). Seismic
794 imaging of the magmatic underpinnings beneath the Altiplano-Puna volcanic complex
795 from the joint inversion of surface wave dispersion and receiver functions. *Earth and*
796 *Planetary Science Letters*, 404, 43-53.
- 797 109. Wessel, P., W. H. F. Smith, R. Scharroo, J. Luis, and F. Wobbe, Generic Mapping Tools:
798 Improved Version Released, *EOS Trans. AGU*, 94(45), p. 409–410, 2013.
799 doi:10.1002/2013EO450001.
- 800 110. Willis, B. (1929). Earthquake conditions in Chile. Carnegie Institution of Washington,
801 382, 178p.
- 802 111. Yáñez-Cuadra, V., Ortega-Culaciati, F., Moreno, M., Tassara, A., Krumm-Nualart, N.,
803 Ruiz, J., ... & Benavente, R. (2022). Interplate coupling and seismic potential in the
804 Atacama Seismic Gap (Chile): Dismissing a rigid Andean sliver. *Geophysical Research*
805 *Letters*, 49(11), e2022GL098257.
- 806
- 807
- 808



812 Figure 1. **a)** Seismotectonic setting of the study area. Solid black lines represent the extent
 813 of historical megathrust earthquakes in the area (Monfret et al., 1995; Ruegg et al., 1996;
 814 Delouis et al., 1997; Delouis et al., 2009; Peyrat et al., 2010; Bejar-Pizarro et al., 2010; Ruiz
 815 and Madariaga, 2018) and white star show the epicenter of the intraplate 1950 Calama
 816 earthquake (Kausel and Campos, 1992). Solid blue and green lines mark the main trend of
 817 the Atacama and Domeyko Fault Systems, respectively. Segmented black lines represent
 818 crustal faults: COT, Calama-Olacapato-Toro; AGF, Achibarca-Galan fault ; TTF, Taltal fault;
 819 MF, Mejillones fault. Red triangles show the active volcanoes and segmented lines offshore
 820 indicate the projection of the Mejillones Fracture Zone (MFZ) and Taltal ridge (TTR). Black
 821 squares highlight major settlements in the region, TOC: Tocopilla, CAL: Calama, SPA: San
 822 Pedro de Atacama, ANF: Antofagasta, TAL: Taltal. **b)** Distribution of the temporary seismic
 823 experiment with 88 short period 4.5 Hz geophones (white triangles) recording at 200 sps.
 824 The network collected data for 8 months, between March and October 2020. Yellow
 825 squares indicate major mining operations in the area. Black squares represent settlements
 826 in the region.

827

828



837 Figure 2. Seismicity distribution for the Taltal segment. **a)** Map view with earthquakes as
 838 small circles colored according to depth. Yellow squares indicate major mining operations
 839 in the area. Red triangles represent the active volcanic arc. The ellipses show the Norwest
 840 lineaments L1, L2, L3 described in text. Black squares show the main settlements. MFZ:
 841 Mejillones Fracture Zone, TTR: Taltal Ridge, APMB: Altiplano-Puna Magmatic Body, LMB:
 842 Lazufre Magmatic Body, SdA: Salar de Atacama. **b)** W-E profiles with the seismic distribution
 843 in depth as shown in scale. Inverted triangles represent the station distribution in the area.
 844 The volcanic arc is represented by red triangles. AFS: Atacama Fault System, DFS: Domeyko
 845 Fault System.

846

847

848

849

850

851

852

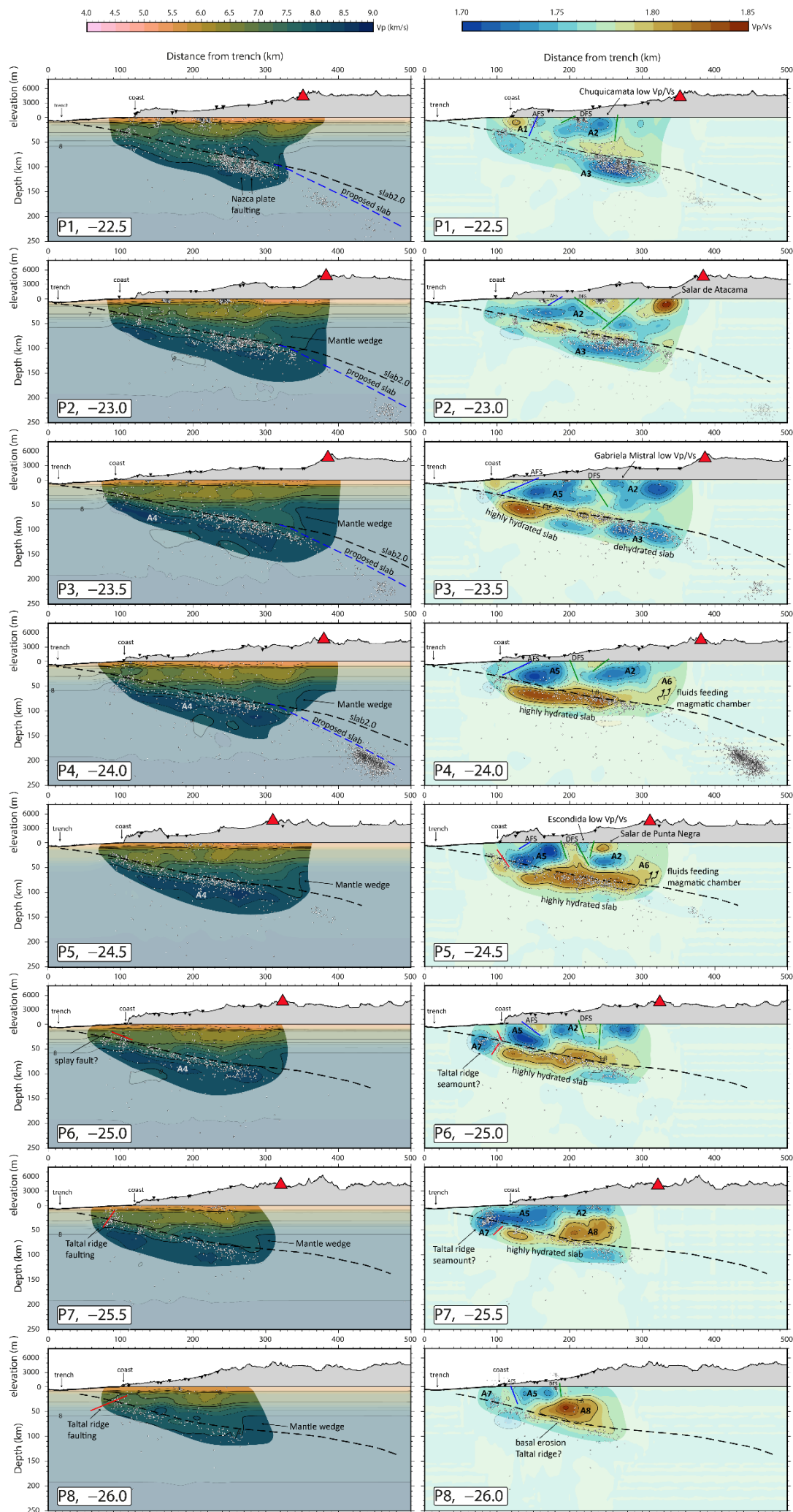


Figure 3. Cross sections of the 3D velocity model for V_p (left) and V_p/V_s (right). Results are shown along 8 W-E profiles shown in Figure 3. V_p velocities and V_p/V_s ratios are color-coded and isocontours are plotted every 0.25 km/s and 0.05 for V_p and V_p/V_s , respectively. Well-resolved areas are highlighted based on the resolution tests. Width for projection of hypocenters and stations is 20 km. Relocated hypocenters are plotted as white circles, and stations are represented by inverted triangles. Proposed slab interface (see text for further details) is represented by segmented blue line while slab 2.0 (Hayes et al., 2018) is shown with segmented black line. Red triangles indicate the position of the volcanic arc. AFS: Atacama Fault System, DFS: Domeyko Fault System; A1-A8, anomalies described in text.

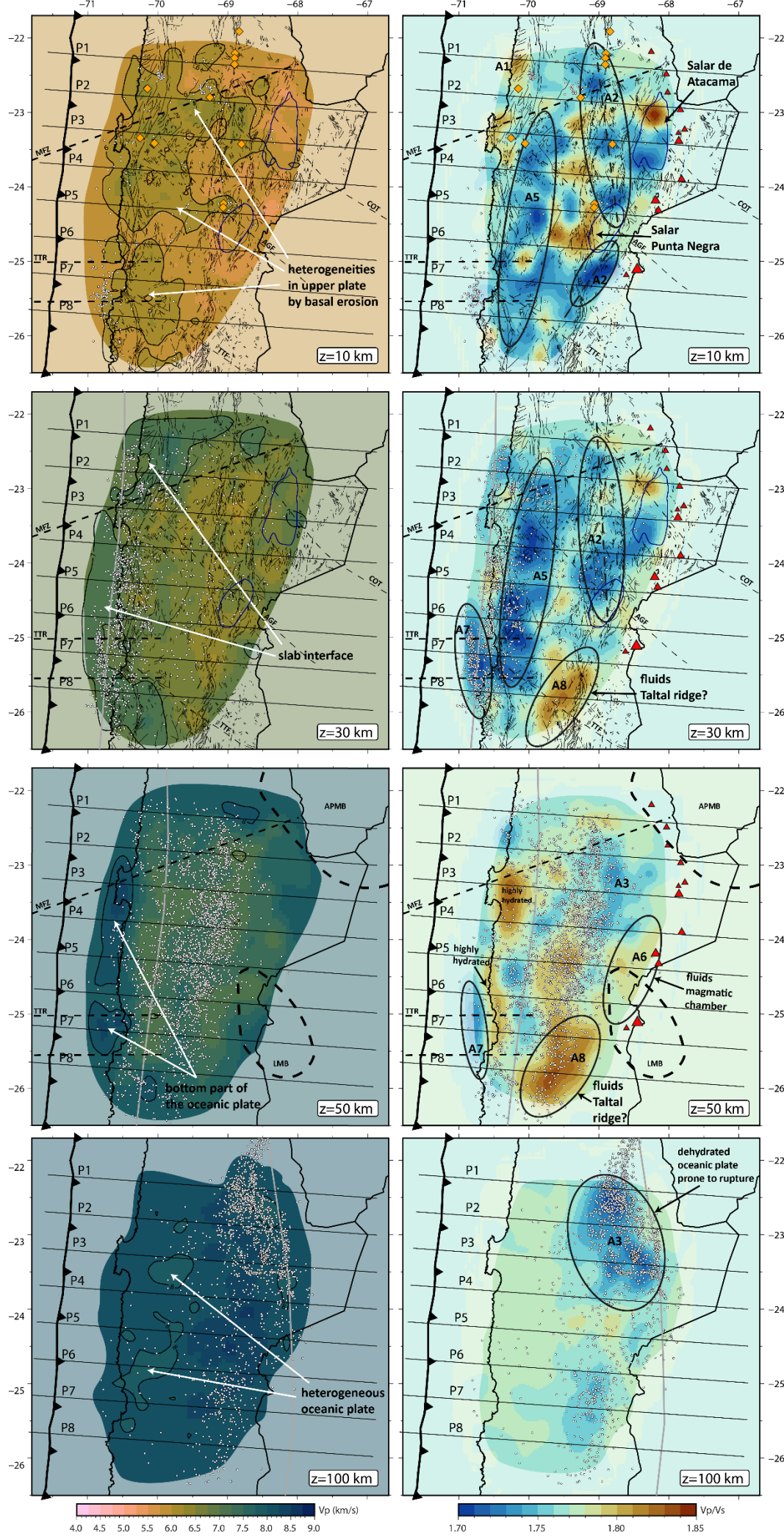


Figure 4. 3D velocity models, V_p (left) and V_p/V_s (right) shown in horizontal slices at 10, 30, 50 and 100 km depth. Well-resolved areas are highlighted based on the resolution tests. Red triangles indicate the position of the volcanic arc. Major mining operations are represented by yellow squares in the 10 km depth slices. Velocity anomalies collocated to surface observations and cities in the text are also shown in the 10 km depth slice. Location of cross section profiles of Figure 3 are shown as black solid lines. Corresponding slab depth contour (Hayes et al., 2018) is represented by a thick gray line. Seismicity is plotted by depth, d , with $d \leq 10$ km in $z = 10$ km, $20 < d \leq 35$ km in $z = 30$ km, $40 < d \leq 55$ km in $z = 50$ km, and $90 < d \leq 110$ km in $z = 100$ km. Fault map is plotted at shallower depths (10-30 km). MFZ: Mejillones Fracture Zone, TTR: Taltal Ridge, APMB: Altiplano-Puna Magmatic Body, LMB: Lazufre Magmatic Body. The anomalies labeled A1-A8, are described in the text.